ADVANCED MATERIALS

Supporting Information

for *Adv. Mater.,* DOI: 10.1002/adma.202200956

Catalytic Growth of Ultralong Graphene Nanoribbons on Insulating Substrates

Bosai Lyu, Jiajun Chen, Shuo Lou, Can Li, Lu Qiu, Wengen Ouyang, Jingxu Xie, Izaac Mitchell, Tongyao Wu, Aolin Deng, Cheng Hu, Xianliang Zhou, Peiyue Shen, Saiqun Ma, Zhenghan Wu, Kenji Watanabe, Takashi Taniguchi, Xiaoqun Wang, Qi Liang, Jinfeng Jia, Michael Urbakh, Oded Hod, Feng Ding,* Shiyong Wang,* and Zhiwen Shi**

Supporting Information

Catalytic growth of ultralong graphene nanoribbons on insulating substrates

Bosai Lyu[1,2†], Jiajun Chen[1,2†], Shuo Lou[1,2†], Can Li[1,2†], Lu Qiu[3,4†], Wengen Ouyang[5†], Jingxu Xie[1,2], Izaac Mitchell[3,4], Tongyao Wu[1,2], Aolin Deng[1,2], Cheng Hu[1,2], Xianliang Zhou[1,2], Peiyue Shen[1,2], Saiqun Ma[1,2], Zhenghan Wu[1,2], Kenji Watanabe[6], Takashi Taniguchi[7], Xiaoqun Wang[1,2,8], Qi Liang[1,2,8], Jinfeng Jia[1,2,8], Michael Urbakh[9], Oded Hod[9*], Feng Ding[3,4*], Shiyong Wang[1,2,8*], Zhiwen Shi[1,2,8*]

[1]Key Laboratory of Artificial Structures and Quantum Control (Ministry of Education), Shenyang National Laboratory for Materials Science, School of Physics and Astronomy, Shanghai Jiao Tong University, Shanghai 200240, China.

[2]Collaborative Innovation Center of Advanced Microstructures, Nanjing University, Nanjing 210093, China.

[3]Centre for Multidimensional Carbon Materials, Institute for Basic Science, Ulsan 44919, South Korea.

[4]School of Materials Science and Engineering, Ulsan National Institute of Science and Technology, Ulsan 44919, South Korea

[5]Department of Engineering Mechanics, School of Civil Engineering, Wuhan University, Wuhan, Hubei 430072, China.

[6]Research Center for Functional Materials, National Institute for Materials Science, 1-1 Namiki, Tsukuba 305-0044, Japan.

[7]International Center for Materials Nanoarchitectonics, National Institute for Materials Science, 1-1 Namiki, Tsukuba 305-0044, Japan.

[8]Tsung-Dao Lee Institute, Shanghai Jiao Tong University, Shanghai, 200240, China.

[9]Department of Physical Chemistry, School of Chemistry and The Sackler Center for Computational Molecular and Materials Science, The Raymond and Beverly Sackler Faculty of Exact Sciences, Tel Aviv University, Tel Aviv 6997801, Israel.

[†]These authors contributed equally to this work.

*Correspondence to: odedhod@tauex.tau.ac.il, f.ding@unist.ac.kr, shiyong.wang@sjtu.edu.cn, zwshi@sjtu.edu.cn

1. Raman mapping and spectra of GNRs and CNTs

2. Large-scale STM topography image of two GNRs

3. The relation of GNR width and nanoparticle size

4. The bandgaps of a series of ZZ- and AC-GNRs of different widths

5. Structural analysis of moiré patterns developing in GNRs placed along different directions of the *h*-BN substrate lattice

6. Competitive nucleation of GNRs and CNTs

7. MD simulations of GNR growth on h-BN

8. A possible mechanism for GNR folding

9. Theoretical analysis of the Schulz-Flory length distribution of the grown GNRs

1. Raman mapping and spectra of GNRs and CNTs

To characterize the graphene nanoribbons (GNRs) and carbon nanotubes (CNTs) grown on the hexagonal boron nitride (*h*-BN) substrate, we performed Raman mapping analysis. Fig. S1a shows the G band intensity mapping, clearly revealing a quasi-one-dimensional bent structure. Fig. S1b shows two Raman spectra (green and blue) taken above the surface areas marked with dashed lines of the corresponding colors. The spectrum taken above the area marked with the blue dashed line shows an asymmetric split G band with a pronounced high frequency peak, characteristic of semiconducting CNTs[1]. The spectrum taken above the area marked with the blue dashed line shows both G and D peaks of comparable intensity, signifying an armchair GNR (AC-GNR).

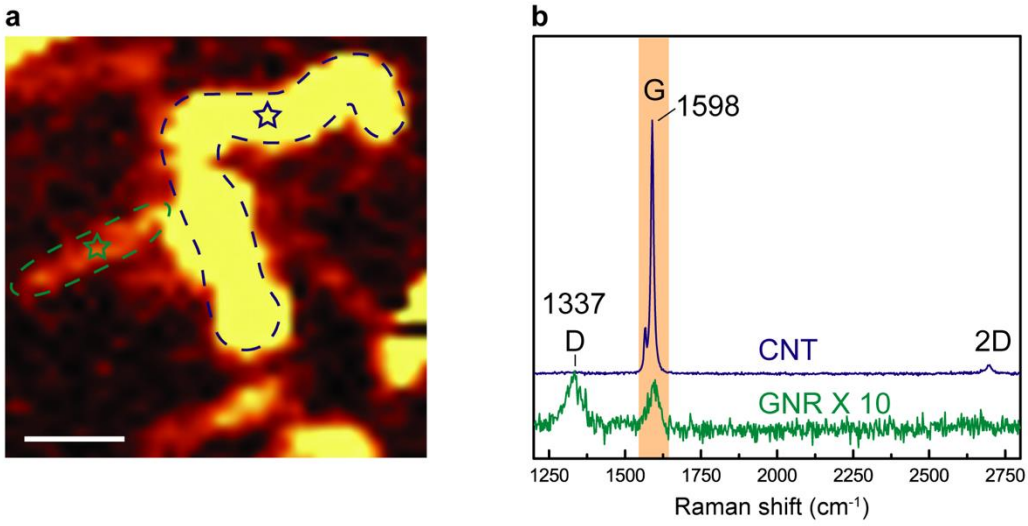

Figure S1. Spectral and structural characterization of the grown quasi-one-dimensional structures. (a) Raman G band intensity mapping of a CNT (enclosed by the blue dashed green) and a GNR (enclosed by the green dashed line) atop of *h*-BN. Scale bar: 500 nm. **(b)** Raman spectra of the CNT (blue) and GNR (green).

2. Large-scale STM topography image of two GNRs

In Fig. 1e of the main text we presented a high-resolution STM image of a short section of one of the grown GNRs. For completeness, we provide here a large-scale STM image of two as-grown GNRs demonstrating that even at micrometer length-scales the GNRs show only minute variations in their width.

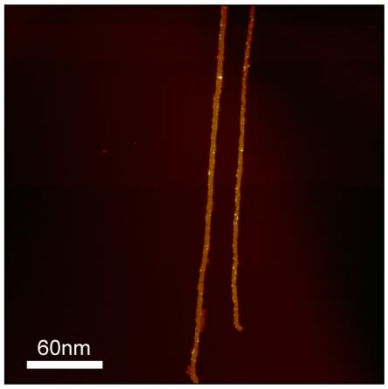

Figure S2. Large-scale STM topography image of two as-grown GNRs (constant current scanning mode at 2V and 10 pA).

3. The relation of GNR width and nanoparticle size

In Fig. 1c of the main text, the widths of the grown GNRs are typically smaller than the dimensions of the nanoparticle on which they are nucleated. To explore the relation between GNR width and nanoparticle size, we present in Fig. S3 a correlation analysis of GNR width and the corresponding catalyst nanoparticle diameter. The data indicate that the GNR width is limited by, and typically smaller than, the nanoparticle diameter. This result is similar to the case of catalytic growth of carbon nanotubes, where the diameter of grown nanotubes is limited by the size of the catalytic nanoparticle[2, 3].

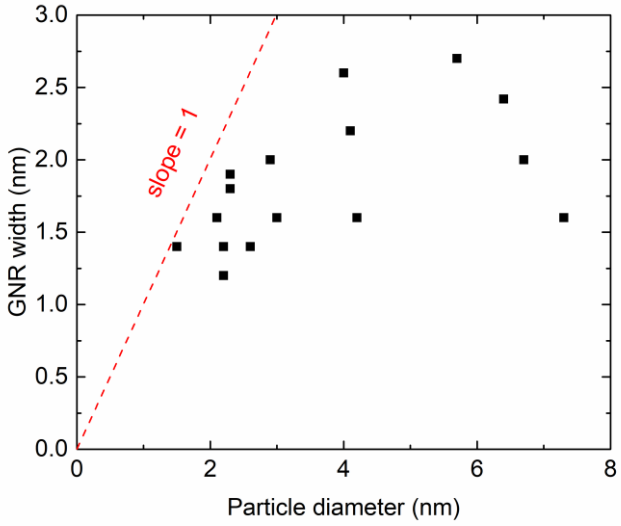

Figure S3. Correlation between GNR width and nanoparticle diameter. The dashed red line indicates equality between GNR width and nanoparticle diameter.

4. The bandgaps of a series of ZZ- and AC-GNRs of different widths

In Fig. 1g of the main text we presented a typical scanning tunneling spectroscopy (STS) measurement for determining the bandgap of a given GNR. Figs. S4 and S5 present STS measurements for more armchair (Fig. S4) and zigzag (Fig. S5) GNRs, allowing us to demonstrate the width dependence of the bandgap appearing in Figs. 1h, i.

We note that under the experimental growth conditions with methane and hydrogen feeding gases there are only two options for GNR edge termination: dangling carbon bonds or hydrogen termination. The former is known to be energetically unfavorable (see, e.g., C. K. Gan et al. Phys. Rev. B, 2010, 81, 125445) hence hydrogen termination is most likely to occur. Moreover, the experimentally observed hydrogen-tunable GNR versus CNT formation ratio provides additional support for hydrogen termination. Therefore, the enhanced electron density localized at some edge regions in the STM scans presented in Figs. S4 and S5 is attributed to post-growth edge oxidation due to unavoidable exposure to air when the sample is transferred from the CVD furnace to the STM chamber.

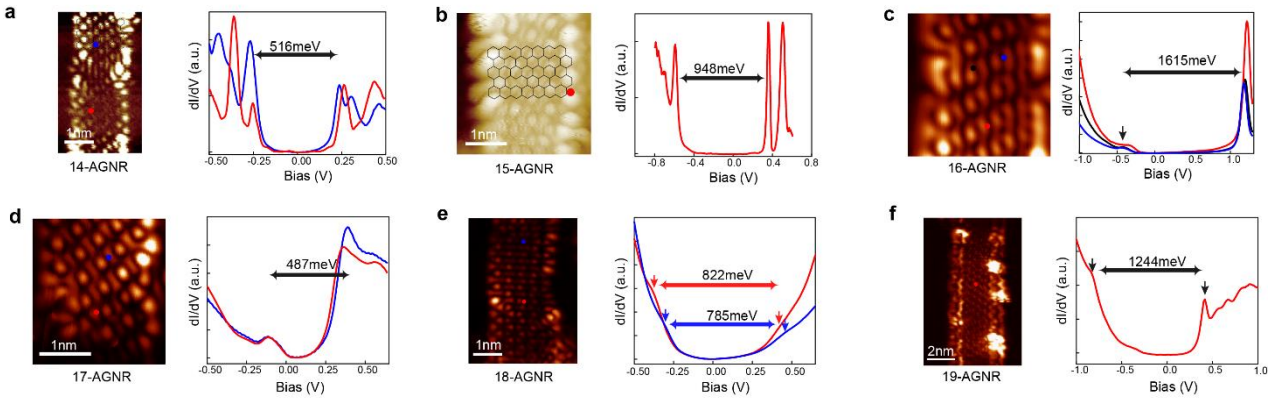

Figure S4. STM images and corresponding dI/dV spectra of the 14-AGNR (a), 15-AGNR (b), 16-AGNR (c), 17-AGNR (d), 18-AGNR (e), 19-AGNR (f). Scanning parameters: (b) constant current mode (V = 100 mV, I = 100 pA); (a, c - f) constant height mode (V = 10 mV).

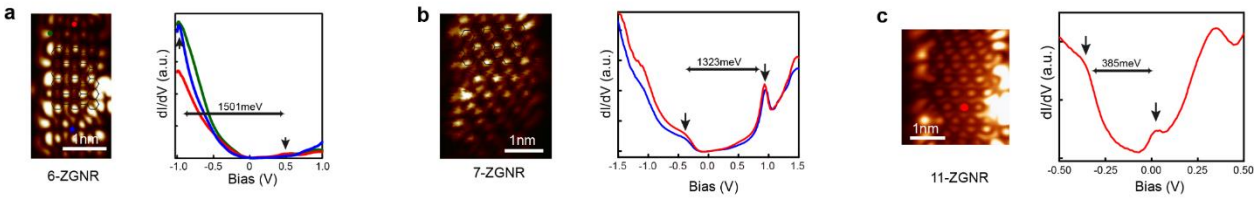

Figure S5. STM constant height current images (bias voltage: 10 mV) and corresponding dI/dV spectra of the 6-ZGNR (a), 7-ZGNR (b), 11-ZGNR (c).

5. Structural analysis of moiré patterns developing in GNRs placed along different directions of the *h*-BN substrate lattice

In the main text, it was mentioned that our observation of a uniform moiré period of $\sim 15\ nm$ indicates that the chirality of the GNRs matches their growth direction along the *h*-BN substrate (see Fig. S6a). To demonstrate this, we performed a set of geometry relaxation calculations (see Section 7.1 and *Method* for detail) of GNRs cut along specific lattice directions and placed atop the *h*-BN substrates at the corresponding orientation angle (see Fig. S6b). The results of the structural relaxation reveal that the moiré period in this case is practically independent of the orientation angle giving a uniform value of $\sim 15\ nm$ (see Fig. S6c). This allows us to assign a chiral angle to each grown GNR according to its orientation relative to the underlying *h*-BN substrate (see Fig. S6d).

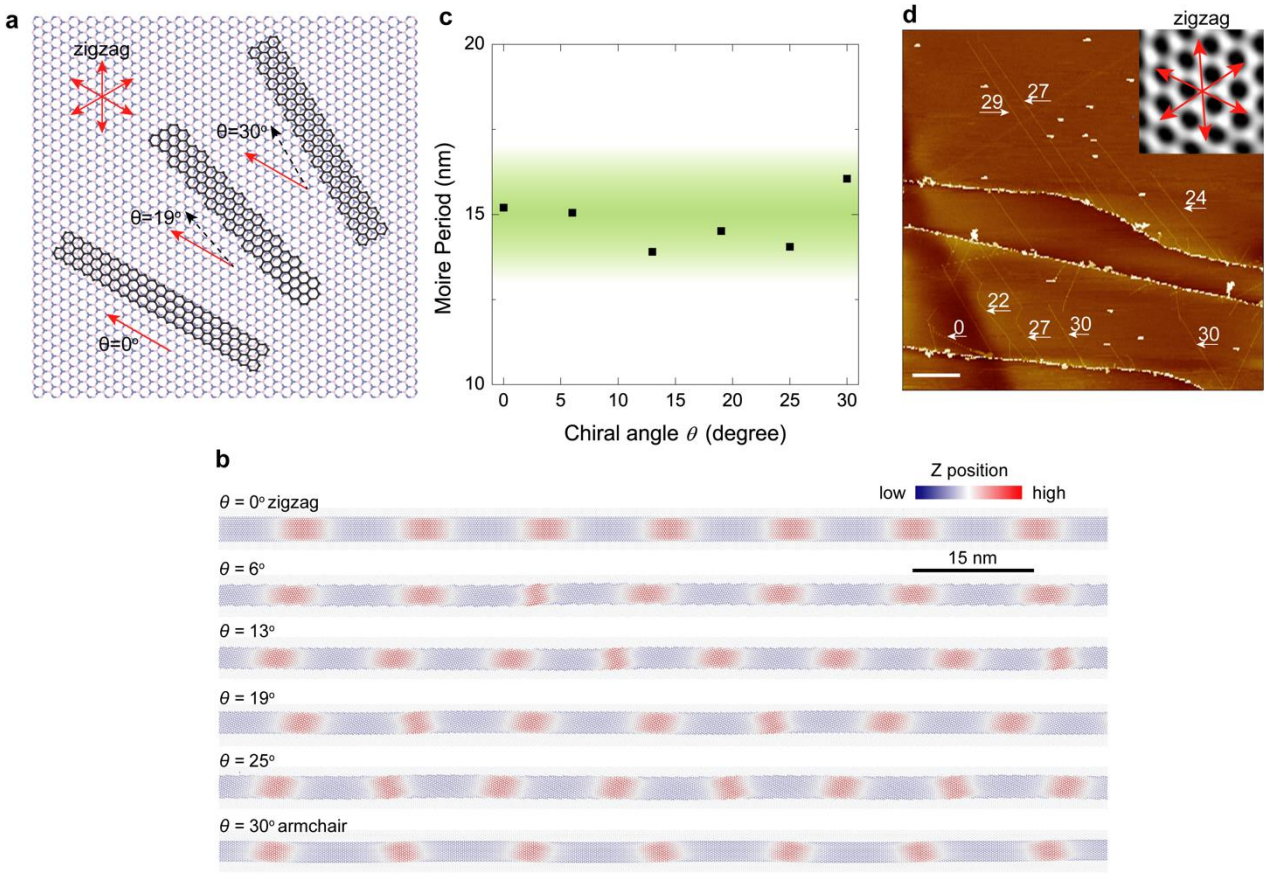

Figure S6. Structural analysis of moiré patterns developing in GNRs placed along different directions of the *h*-BN substrate lattice. (a) Illustration of epitaxial growth of GNRs atop an *h*-BN substrate, where matching between the GNR chirality and growth orientation is observed. **(b)** out of plane atomic displacement for GNRs laying atop an *h*-BN substrate. The GNRs are cut along the following crystal orientations, $\theta = 0^{\circ}$ (zigzag), 6°, 13°, 19°, 25°, and 30° (armchair), and placed at the corresponding *h*-BN substrate lattice directions. **(c)** moiré periods as a function of chiral angle θ in degrees extracted from the results presented in panel a. **(d)** assignment of GNR chiral angles according to their orientation with respect to the underlying *h*-BN substrate, scale bar: 500 nm.

6. Competitive nucleation of GNRs and CNTs

a. Phase diagram

To investigate the competitive formation of GNR and CNT on an *h*-BN substrate we performed DFT calculations (see Methods section) on the periodic model systems presented in Fig. S7. A hydrogen passivated armchair (AC) GNR model was placed onto a bilayer *h*-BN slab applying periodic boundary conditions along both lateral directions with supercell dimensions of 4.29×39.68×18.00 Å^3 (see Fig. S7a). During the calculations the bottom substrate model layer was kept fixed. The formation energy of an AC-GNR of a given width (W) was calculated according to the following equation:

$$E_f^{GNR} = E_{tot} - E_{sub} - N_c \times E_C - \frac{1}{2} N_H \times E_{H_2} \quad \text{(S1)}$$

where E_{tot}, E_{sub}, N_c, E_C, N_H, and E_{H_2} represent the total energy of the supercell, the energy of the substrate, the number of the carbon atoms in the GNR, the reference energy of the carbon atoms (*i.e.* the energy of carbon atom in graphene -9.3310 eV/atom), the number of the hydrogen atoms at the GNR edge, and the energy of a hydrogen molecule (-6.7959 eV/molecule).

Similarly, the formation energy of a CNT of a given diameter (d) was calculated for a 4.29×39.68×28.00 Å^3 supercell (Fig. S7b) using the following equation:

$$E_f^{CNT} = E_{tot} - E_{sub} - N_C \times E_C \quad \text{(S2)}$$

To reduce computational burden, these calculations were performed for five narrow AC-GNRs and CNTs (see Table. S1) and the results were extrapolated to the experimentally relevant dimensions. For AC-GNRs, a linear fit of the following form was used (see Fig. S8a):

$$E_f^{GNR}(W) = 0.17243 - 077297 \times W \quad \text{(S3)}$$

where the first term represents the edge energy of the AC-GNR and the second term accounts for the Van der Waals interaction (both for per unit cell length 4.29 Å). With this fitting equation, we could estimate the formation energy of AC-GNRs with any widths on *h*-BN substrate. For example, in our experiments the width of the synthesized AC-GNR is usually ~ 2.2 nm (Fig. 1f), and therefore the formation energy should be -1.53 eV per unit cell length according to Eq. S3.

The fitting line for the formation energy of CNT as a function of the diameter d is presented in Fig. S8b using the following equation:

$$E_f^{CNT}(d) = \frac{4.0010}{d} - 0.2933 \times \sqrt{d} \quad \text{(S4)}$$

where the first term denotes the curvature energy, which is inversely proportional to the CNT diameter. The second term represents the van der Waals interaction energy with the underlying substrate, which is proportional to the square root of the CNT diameter. As illustrated in Fig. S7b, if we assume that the effective van der Waals interacting height h-h_0 is a constant, e.g., $h_0/3$, the real effective interacting length L between the CNT wall and the h-BN substrate will be proportional to $\sqrt{d}$. Therefore, with this equation, we can now also estimate the formation energy of CNT with any diameter on h-BN substrate.

To understand the competitive formation of AC-GNR and CNT, we need to compare the formation energies of an AC-GNR with a specific width and a CNT with a specific diameter. As the synthesized GNRs and CNTs are generally with a width (GNR) to diameter (CNT) ratio (W/d) of ~1.6-2.1 (Fig. 1f and Fig. S9), we therefore proposed an effective ratio of 1.88 for the following calculation and comparison (W=1.88d). This means that we compare the formation energies of an AC-GNR with a width of W and a CNT with a diameter of d=W/1.88.

Since the DFT calculations consider only the ground state (at 0 K) formation energies, we evaluated the free energies of formation of GNRs and CNTs at the experimental conditions by including the influence of a heat bath temperature and external pressure. Notably, the intrinsic vibrational entropy of the sp^2 carbon lattice in GNRs and CNTs as well as the entropy associated with the h-BN substrate are similar for both systems. Hence, the main entropy term that influences the thermodynamic stability difference between the two systems is associated with the hydrogen termination of the GNRs. This free energy contribution was therefore estimated via the difference between the vibrational entropy of the hydrogen termination at the GNR edges (ΔF_{vib}) and the hydrogen chemical potential in the gas phase under the experimental conditions (μ_{H_2}), calculated using the following equation:[4, 5]

$$\Delta G_f(GNR) = E_f(GNR) + \Delta F_{vib} - \frac{1}{2} N_H \times \mu_{H_2} \quad \text{(S5)}$$

The vibrational term ΔF_{vib} was estimated according to the following equation:[6]

$$\Delta F_{vib} = \sum_{\omega} h\omega \left(\frac{1}{2} + \frac{1}{e^{\beta h\omega} - 1}\right) - kT \left(\frac{\beta h\omega}{e^{\beta h\omega} - 1} - \ln\left(1 - e^{-\beta h\omega}\right)\right) \quad \text{(S6)}$$

where the vibrational frequencies of the edge C-H bonds were obtained from the DFT calculations (see Table. S1). The hydrogen chemical potential was estimated from the NIST-JANAF Thermochemical tables[7] and the hydrogen pressure in the experiments according to the following equation:[5]

$$\mu_{H_2} = H^0(T) - H^0(0) - TS^0(T) + k_b T ln\left(\frac{p_{H_2}}{p^0}\right) \quad \text{(S7)}$$

The obtained free energies of formation of AC-GNRs and CNTs on *h*-BN as a function of the hydrogen partial pressure logarithm are presented in Fig. S8c. By extracting the crossing points between the free energies of formation of the AC-GNRs and CNTs at different temperatures we constructed the phase diagram appearing in Fig. 3d of the main text. The same procedure was used to construct the phase diagram of ZZ-GNR vs. CNT as shown in Fig. S10 (see also Table. S1), which shows similar trends.

The above phase diagrams were plotted taking the experimentally observed CNT diameter (1.2 nm) and GNR width (2.2 nm). To evaluate the generality of our results, we repeated the calculations for other system dimensions. Firstly, we plotted the phase diagrams of both ZZ-GNR vs CNT and AC-GNR vs CNT with different width-to-diameter ratios (W/d) as presented in Fig. S10c. It is found that the there is always the same dependence of the relative stability of GNR vs CNT on the temperature and partial hydrogen pressure but only moves the transition line toward the GNR or CNT region slightly. Secondly, we kept the ratio between the GNR width and CNT diameter at 1.88 and plotted the corresponding phase diagrams as presented in Fig. S11. The diagrams indicate that for very wide GNR or CNT (large W), the growth of GNR is more favorable as the van der Waals interaction becomes the dominating component, and for very narrow GNR or CNT (small W), the growth of CNT is prohibited as the curvature energy is enormous at this circumstance.

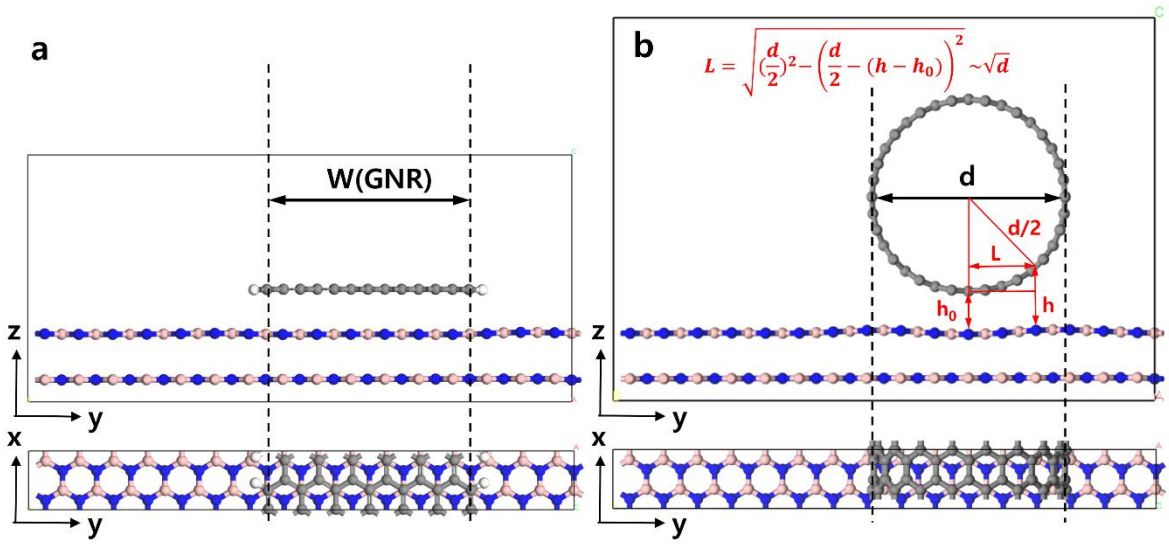

Figure S7. Atomistic models used in the DFT calculations of the formation energies of (a) a GNR and (b) a CNT lying atop a bilayer *h*-BN substrate. The bottom layer of the substrate is kept fixed during the calculations. The stacking order for *h*BN-*h*BN and graphene-*h*BN are AA' and AB, respectively. Grey, white, blue, and pink spheres denote carbon, hydrogen, nitrogen, and boron atoms, respectively.

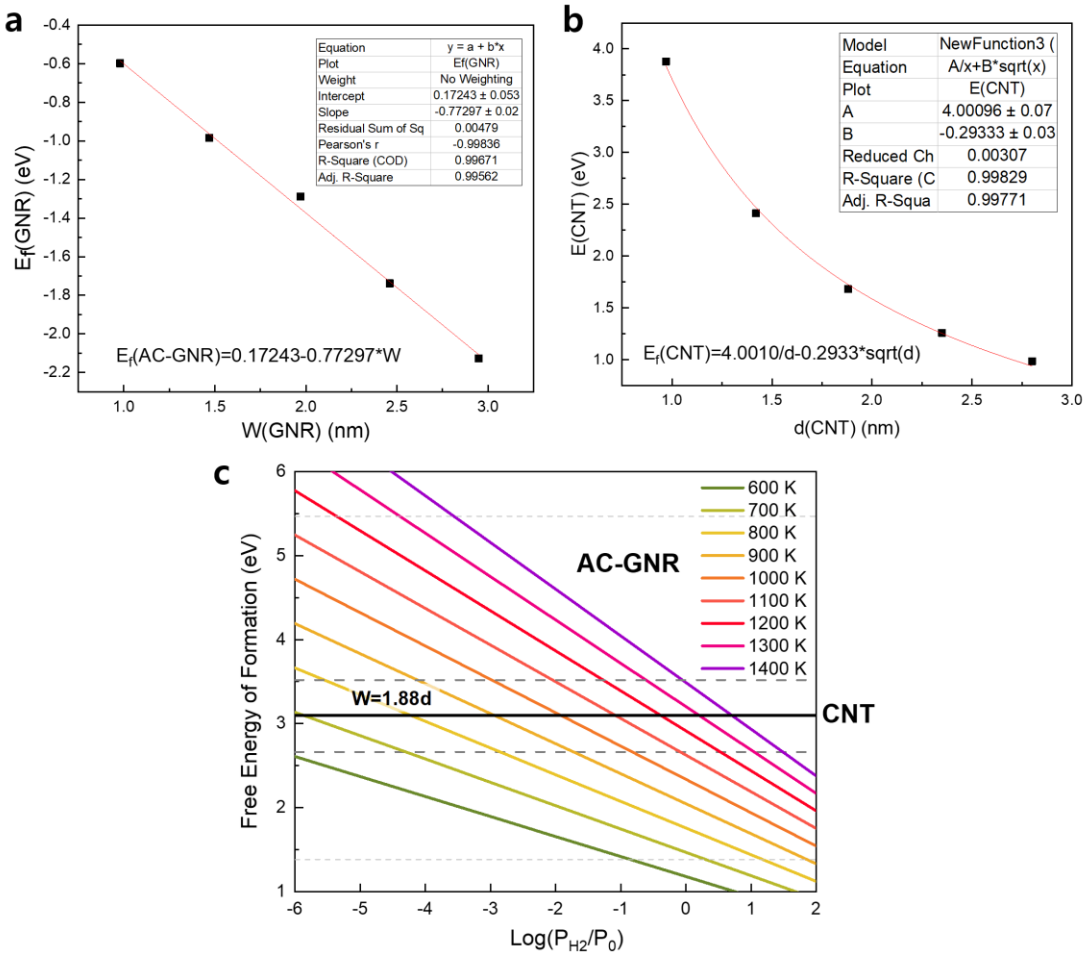

Figure S8. (a) Linear fitting of the AC-GNR formation energy $E_f^{GNR}(W)$ as a function of its width (see Eq. S3). (b) Fitting of the CNT formation energy $E_f^{CNT}(d)$ as a function of its diameter (see Eq. S4). (c) Free energy of formation plot of the AC-GNR (colored lines) and CNT (black line) as a function of the logarithm of the partial hydrogen pressure, calculated at various temperatures (K). Here the width of AC-GNR is ~2.2 nm, and the width-to-diameter ratio (W/d) is ~1.88.

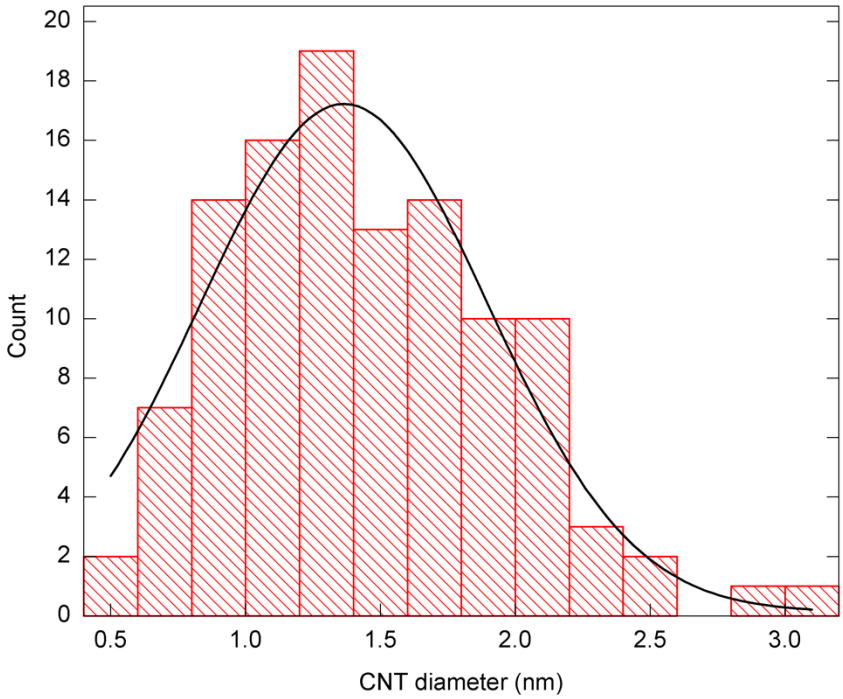

Figure S9. Diameter distribution of carbon nanotubes on *h*-BN measured by AFM.

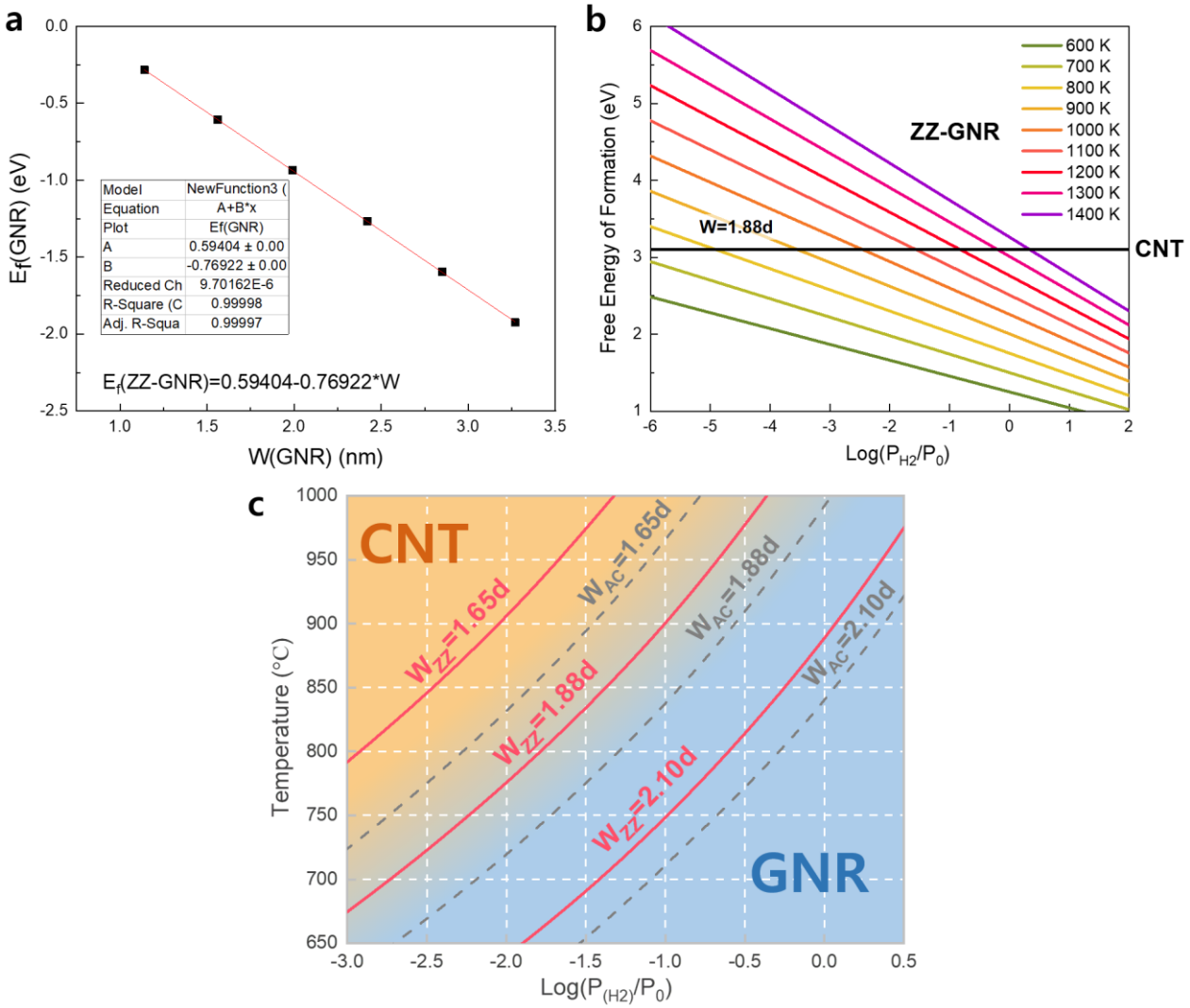

Figure S10. (a) Linear fitting of the ZZ-GNR formation energy $E_f^{GNR}(W)$ as a function of its width. (b) Free energy of formation plot of the ZZ-GNR (colored lines) and CNT (black line) as a function of the logarithm of the partial hydrogen pressure, calculated at various temperatures (K). (c) Phase diagram of the competitive formation of both ZZ-GNR/CNT (pink line) and AC-GNR/CNT (grey dash line) atop an *h*-BN bilayer substrate plotted at the temperature-partial hydrogen pressure space with different width-to-diameter ratios.

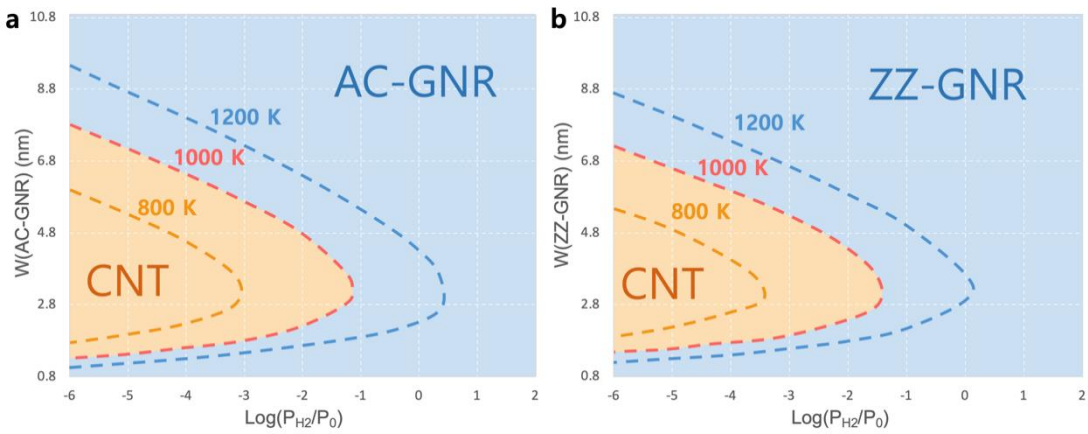

Figure S11. (a) Phase diagram of the formation of AC-GNR vs. CNT on *h*-BN substrate as a function of the width of the AC-GNRs/CNTs (nm) and the hydrogen partial pressure (P_{H2}/P_0) at 800 K (yellow line), 1000 K (red line), and 1200 K (blue line). (b) Phase diagram of the formation of ZZ-GNR vs. CNT on *h*-BN substrate as a function of the width of the ZZ-GNRs/CNTs and the hydrogen partial pressure at 800 K (yellow line), 1000 K (red line), and 1200 K (blue line). Here the ratio of the width of GNR to the diameter of the CNT is ~1.88.

Table S1. Formation energy of GNR (both AC and ZZ) and CNT on *h*-BN substrate as a function of the GNR width W(GNT) and the CNT effective width W(CNT), which is proportional to its diameter d(CNT).

d(CNT) (nm)	W(CNT) (nm)	Ef(CNT) (eV)		
0.97	1.8236	3.8789		
1.42	2.6696	2.4124		
1.88	3.5344	1.6805		
2.35	4.418	1.2583		
2.8	5.264	0.9846		
W(AC-GNR) (nm)	**E_f(AC-GNR) (eV)**	**v(C-H) (THz)**	**v(C-H) (THz)**	**v(C-H) (THz)**
0.98	-0.5977	92.37066	37.00228	19.96064
1.47	-0.9846	91.6587	34.97222	19.6818
1.97	-1.289	91.43748	34.62189	
2.46	-1.7382	91.08105	23.47562	
2.95	-2.1266	37.09185	23.22102	
W(ZZ-GNR) (nm)	**E_f(ZZ-GNR) (eV)**	**v(C-H) (THz)**		
1.14	-0.2842	89.804631		
1.56	-0.6072	89.610926		
1.99	-0.935	36.630741		
2.42	-1.2659	36.54404		
2.85	-1.5947	22.931065		
3.27	-1.9255	22.859075		

b. DFTB simulation of microscopic process of GNR nucleation

The detailed microscopic process of the nucleation of GNRs and the effects of hydrogen was investigated via self-consistent charge density functional tight binding (SCC-DFTB) MD calculations. Within these calculations, when the ratio to C:H atoms was 10:0 (no hydrogen), growth on the Fe nanoparticle either resulted in encapsulation or the growth or a nanotube cap with C atoms aggregating to one side of the Fe nanoparticle (Fig. S12a and d). This process generally followed the initial formation of dimers on the surface followed by sp hybridized C chains as carbon concentrations on the surface increases. These carbon chains increase in size until initial ring formation and the formation of sp^2 carbon. Ring formation then facilitates the formation of further rings resulting in a cap structure to one side of the Fe_{32} nanoparticle that would either lift enough to keep some of the particle exposed or encapsulate the particle.

When the C:H ratio is increased to 10:5 the mechanism for early nucleation remains roughly the same as the sp hybridized C chain lengths do not tend to hydrogenate easily in these conditions. However, once a ring is nucleated the H atoms quickly passivate the now sp^2 hybridized carbon. This leads to a flattening of the sp^2 network as shown in Fig. S12b and S12e as passivation reduces the edge energy resulting in curvature becoming less pronounced, but still present. This leads to the scenario similar to those observed experimentally in intermediate hydrogen concentrations (Fig. 3f) where both CNT caps (Fig. S12b) and passivated GNR flakes (Fig. S12e) are nucleated. Increasing the C:H ratio to 10:10 results in the nucleation of multiple small nanoflakes (Fig. S12c and S12f) with no CNT cap structure observed in our calculations, though some flakes did sit parallel to the Fe_{32} surface (Fig. S12f).

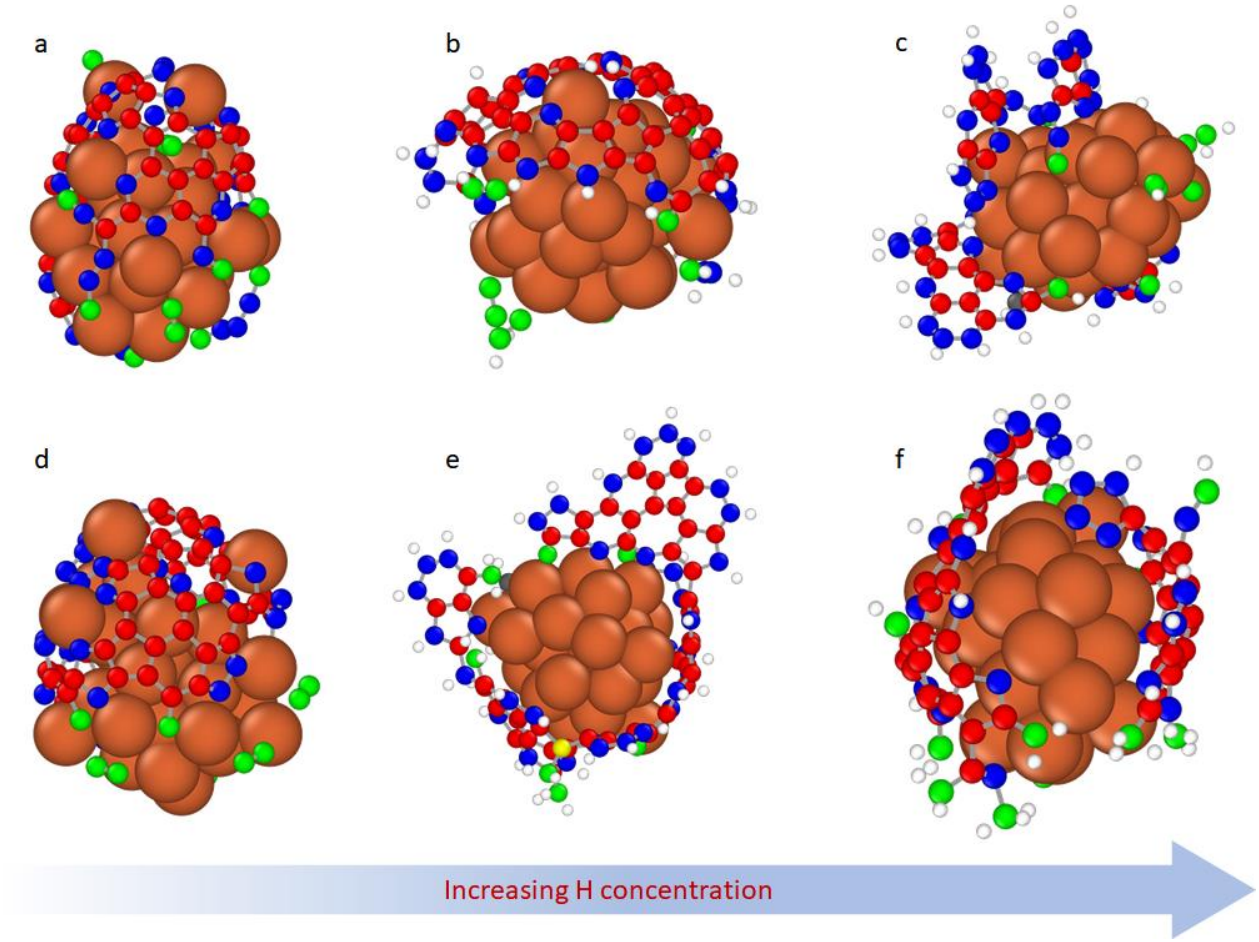

Figure S12 Nucleoforms during CNT/GNR nucleation. a and **d**, at C:H ratios of 10:0, with no hydrogen present nucleation forms cap structure on the Fe_{32} nanoparticle. **b, e** increasing the C:H ratio to 10:5 edge passivation by hydrogen lowers the effects of edge energy, allowing for flatter structure to form. Both CNT caps (b) and GNR flakes (e) are observed in this regime. **c,f** when the C:H ratio is increased to 10:10 edge passivation is more significant allowing for the formation of multiple nanoflakes either vertically (c) or parallel (f) to the Fe_{32} surface. Orange, and white spheres are Fe and H respectively, green, blue, red and yellow spheres are C atoms connected to 1, 2, 3 or 4 other C atoms respectively.

Movie S1 Nucleation of defective CNT cap at very low or zero hydrogen (C:H ratio of 10:0) environments the carbon generally either forms a cap or encapsulated the nanoparticle. Orange

spheres are Fe while green, blue, red and yellow spheres are C atoms connected to 1, 2, 3 or 4 other C atoms respectively.

Movie S2 Nucleation of GNR/CNT hybrid at intermediate levels of hydrogen (C:H ratio of 10:5) the nucleation process will yield with GNR like structures or CNT like structures. Sometimes this process yields a structure that shows signs of both nucleation modes as exemplified by this movie. Orange spheres are Fe and white are H while green, blue, red and yellow spheres are C atoms connected to 1, 2, 3 or 4 other C atoms respectively.

Movie S3 Nucleation of multiple GNRs at high hydrogen concentrations (C:H ratios of 10:10) the nucleation process yields only GNR structures that often sit up perpendicular to the nanoparticle surface. Occasionally, this will yield multiple GNR structures on the same nanoparticle. Orange spheres are Fe and white are H while green, blue, red and yellow spheres are C atoms connected to 1, 2, 3 or 4 other C atoms respectively.

7. MD simulations of GNR growth on *h*-BN

7.1 Model system preparation

The simulated model system consists of an AC-GNR or ZZ-GNR of fixed width (~2 nm) and of various lengths in the range of 5-1000 nm sliding along the armchair (zigzag) direction of the bilayer AA'-stacked *h*-BN substrate, of which the bottom layer is kept fixed (see Figure S13). The GNRs' edges are passivated by hydrogen atoms[8] to avoid peripheral C–C bond reconstruction[9, 10], that may influence friction. The intra-layer interactions within the GNRs and *h*-BN were computed via the second generation of REBO potential[11] and the Tersoff potential[12], respectively. The interlayer interactions between the GNRs and the *h*-BN substrate were described via the registry-dependent interlayer potential (ILP)[13-15] with a refined parametrization[16], which is implemented in the LAMMPS[17] suite of codes. The starting system configurations were generated via geometry optimization of the GNR atop the *h*-BN substrate using the FIRE algorithm[18] as implemented in LAMMPS[17], with a force threshold value of 10^{-6} eV/Å. The resulting GNR height profile were found to be in good agreement with the experimental data (see Figure 2c of the main text).

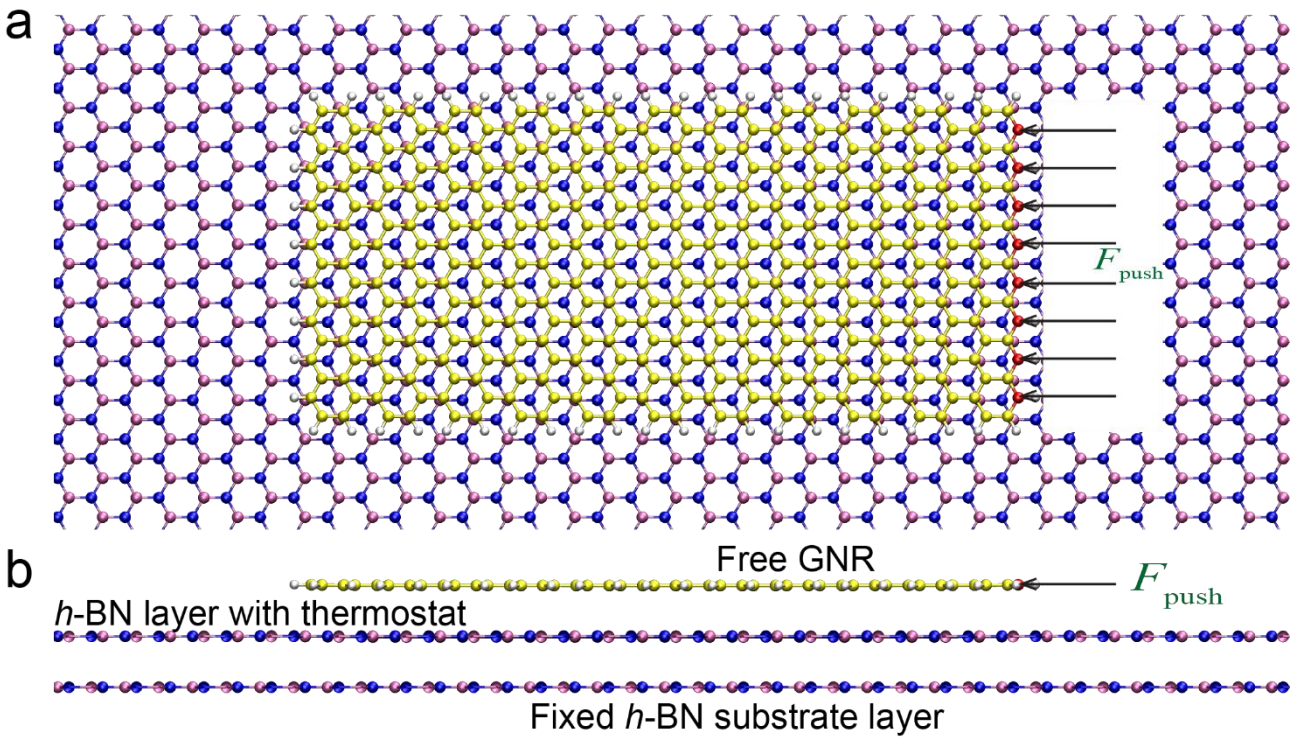

Figure S13. Schematic representation of the simulation setup: **a** top view and **b** side view. A graphene nanoribbon deposited over a bilayer AA'-stacked *h*-BN substrate is pushed by a constant

force applied to the rightmost carbon atoms (red spheres). Mauve, blue, yellow, and gray spheres represent boron, nitrogen, carbon, and hydrogen atoms, respectively.

7.2 Sliding dynamics and friction at zero temperature

The results presented in the main text, show friction forces evaluated at the experimental growth temperature of 1073 K. To better understand the underlying mechanism and examine the effect of temperature on the frictional properties of the GNR/*h*-BN heterojunction, we repeated the MD simulations at zero temperature. To this end, we applied a constant lateral pushing force to the rightmost carbon atoms of the preoptimized GNRs (see Figure S13a), implementing a damping constant of $1\ \mathrm{ps}^{-1}$ to all atoms residing in the top (flexible) layer of the *h*-BN substrate and keeping the bottom substrate layer fixed (Figure S13b). To evaluate the static friction force, a set of consecutive simulations under constant pushing force were performed. After each such 500,000 time-steps (0.5 ns, with a time step of 1 fs) simulation the pushing force was increased by 0.125 or 0.25 nN until the GNR started sliding. The static friction force was then defined as the average of the pushing force values applied during the two simulations right before and right after sliding commenced.

Figure S14 shows the length dependence of the calculated static friction force for both AC-GNRs and ZZ-GNRs aligned along the armchair and zigzag direction of a bilayer AA'-stacked *h*-BN substrates at 0 K, respectively. The static friction force at 0 K is found to be ~2 times larger than that at 1073 K (see Fig. 4e of the main text), which indicates that thermal activation plays a significant role in friction reduction in this system.

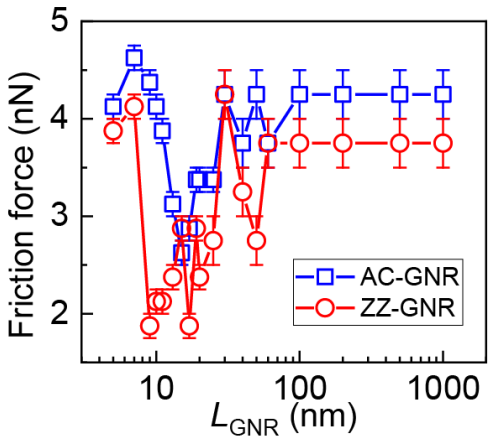

Figure S14. Length dependence of the static friction force of armchair (open blue squares) and zigzag (open red circles) GNRs sliding atop a bilayer AA'-stacked *h*-BN substrate at 0 K.

7.3 The effect of damping constant on the friction force

To avoid system heating during the dynamical simulation we applied phenomenological Langevin thermostats. While these should control the heat flow generated by the sliding contact, they should not influence the frictional characteristics of the system. To this end, we have adopted a bilayer *h*-BN substrate model, where the lower support layer was kept fixed during the dynamics and the upper layer, to which the Langevin thermostat was applied, formed a flexible contact with the sliding GNRs. To verify that the Langevin damping constant has negligible effect on the calculated frictional properties in our simulation setup we repeated the calculations with a value of $0.1\ \mathrm{ps}^{-1}$. Fig. S15 demonstrates that indeed the calculated friction forces of both AC-GNRs (panel (a)) and ZZ-GNRs (panel (c)) of increasing length are practically independent of the damping constant value in the wide range considered. Notably, when applying the Langevin thermostat directly on the AC-GNR (panel (b)) or ZZ-GNR (panel (d)) sliding atop a fixed *h*-BN layer, strong dependence of the results on the value of the damping constant is found.

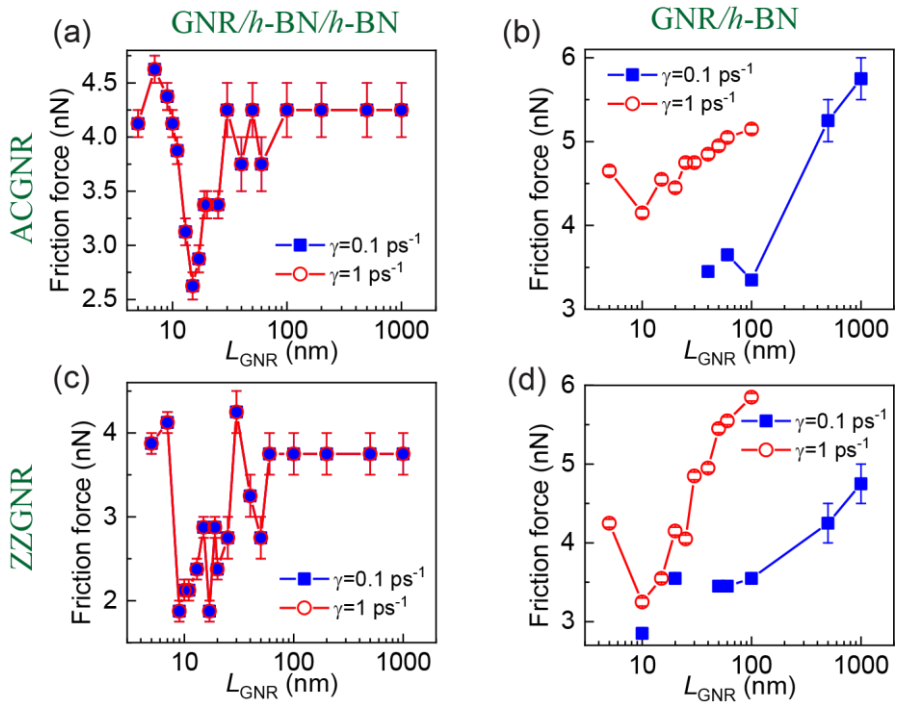

Figure S15. Effect of damping coefficient used in the Langevin thermostat on the friction force calculated for (a, c) a bilayer *h*-BN substrate model with a fixed lower supporting layer and a flexible upper layer, to which the Langevin thermostat is applied when facing the sliding AC-GNR (a) or ZZ-GNR (c); and (b, d) a fixed single *h*-BN layer substrate model, where the Langevin thermostat is applied directly to the sliding AC-GNR (b) or ZZ-GNR (d).

7.4 The effect of lateral buckling on the friction force

In Fig. 4e of the main text, we demonstrated that the static friction forces calculated for AC-GNRs are generally smaller than those of ZZ-GNR when the length of the GNR is smaller than one moiré period atop the *h*-BN substrate. A possible mechanism that may lead to these differences is sideways lateral buckling of the GNR that balances between interlayer adhesion via lattice registry and intralayer tension[16]. Such buckling is indeed found in the AC-GNR considered, but is energetically unfavorable for the corresponding ZZ-GNR. This additional degree of freedom may allow the sliding AC-GNRs to circumvent high energy barriers during the sliding motion, thus reducing both static and dynamic friction. To evaluate the effect of sideway buckling on the static friction, we repeated our 0K calculations while freezing the atomic motion along the lateral direction perpendicular to the GNR main axis. The results, presented in Fig. S16, show that the additional constraint considerably increases the friction calculated for the AC-GNRs whereas its

effect on the ZZ-GNRs friction is minor. This indicates that lateral buckling plays an important role in reducing the friction force of AC-GNRs atop *h*-BN.

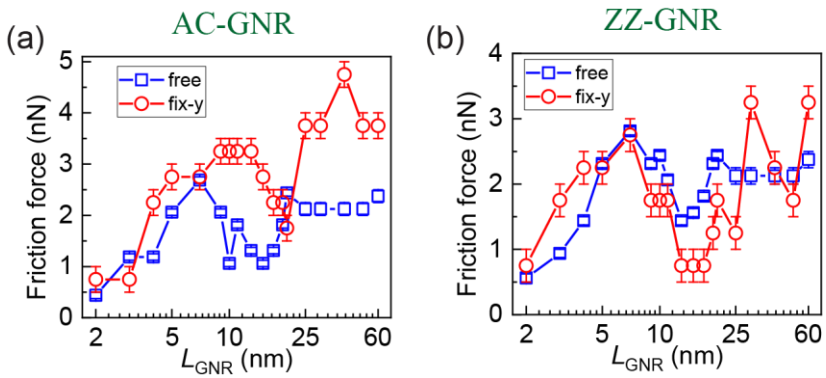

Figure S16. Effect of lateral buckling on the 0 K static friction force calculated for (a) AC-GNR and (b) ZZ-GNR sliding atop a bilayer *h*-BN substrate model with the lower support layer kept fixed.

8. A possible mechanism for GNR folding

In Fig. 4c of the main text we presented a peacock-like structure formed by dynamical folding of the grown GNRs due to surface obstacles. To demonstrate a possible mechanism for such kink formation, we performed MD simulations of a GNR being pushed onto a rigid bilayer *h*-BN step (representing a surface obstacle). In these simulations, the GNR is initially deposited on an *h*-BN surface with its long axis oriented 45° with respect to the zigzag direction of the *h*-BN substrate. In these simulations, damped dynamics is performed for all atoms of the GNR with a damping constant 1 ps^{-1} and a simulation time step of 1 fs, whereas all *h*-BN layers (including the bilayer step) are kept fixed. The adopted force fields are the same as those used in the main text. A constant pushing force of 3 nN is applied to the back end (one atomic row) of the GNR.

As shown in Fig. S17 and in Supplementary Movie 4, once the leading edge of the GNR arrives at the obstacle, further pushing results in its sliding along the *h*-BN step edge and rotation of the entire GNR front section. The back GNR section, being pushed along the original directions, eventually buckles and forms a kink. Naturally, this simple realization represents only one of many possible obstacle-induced GNR kink formation mechanisms during growth.

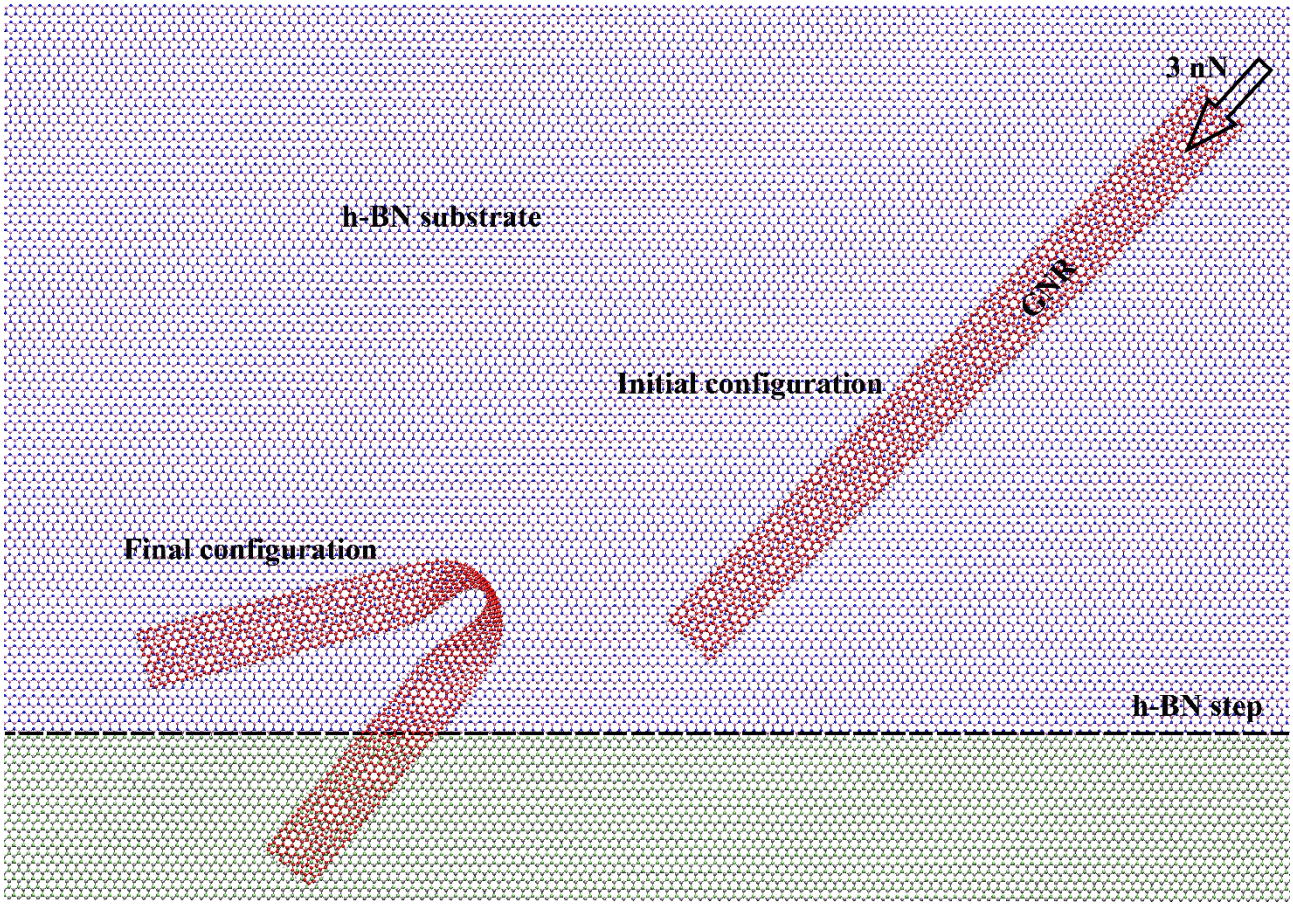

Figure S17. The dynamics of a 20 nm long GNR atop an *h*-BN substrate with a bilayer *h*-BN step. A constant pushing force with a magnitude of 3 nN is applied to the back end of the GNR. Initial (right) and final (left) configurations of the GNR are presented. Mauve and lime spheres represent boron atoms of the substrate and the step regions, respectively. Blue and silver spheres represent nitrogen atoms of the substrate and the step regions, respectively. Red and gray spheres represent carbon and hydrogen atoms, respectively.

9. Theoretical analysis of the Schulz-Flory length distribution of the grown GNRs

The measured length distribution of the grown GNRs was found to match the Schulz-Flory distribution function. This, in turn, provides important insights regarding the catalytic growth process. Here, one may assume that each catalytic center promotes the growth of at most one GNR. Once the growth process initiates, it proceeds until the catalyst becomes deactivated, after which no additional growth can occur at this specific catalytic center. To simplify the treatment, it is further assumed that the GNR growth process occurs in discrete steps, each consisting of the addition of a single carbon row to the GNR edge that is attached to the surface of the catalyst. If the probability, α, for the catalyst to form a new row when the precursor atoms arrive at its surface is independent of the length of the ribbon, the fraction of nanoribbons consisting of n rows is then given by $P_n \propto \alpha^n(1-\alpha)$, where $(1-\alpha)$ is the probability of growth termination. Marking by $d = 2.13$ Å the GNR length addition associated by a single carbon row, the normalized probability to obtain a GNR of length $L = n \times d$ is given by $P_L \propto N_0 \alpha^{L/d}(1-\alpha)$, where $N_0 = 333$. By fitting the measure length distribution to this equation, we can evaluate the probability for a row addition event at the catalyst surface to be $\alpha = 0.99985$. The good agreement between the measured length distribution and the Schulz-Flory probability function thus indicates that the catalytic GNR growth process occurs at a constant rate.

References

[1] M. S. Dresselhaus, A. Jorio, M. Hofmann, G. Dresselhaus, R. Saito, Nano Letters 2010, 10, 751.

[2] M. He, X. Wang, S. Zhang, H. Jiang, F. Cavalca, H. Cui, B. Wagner Jakob, W. Hansen Thomas, E. Kauppinen, J. Zhang, F. Ding, Science Advances, 5, eaav9668.

[3] M. Kumar, Y. Ando, J Nanosci Nanotechnol 2010, 10, 3739.

[4] H. Shu, X. Chen, F. Ding, Chemical Science 2014, 5, 4639.

[5] J. Gao, F. Ding, The Journal of Physical Chemistry C 2015, 119, 11086.

[6] K. Reuter, M. Scheffler, Physical Review B 2001, 65, 035406.

[7] M. Chase, American Institute of Physics, New York 1998.

[8] S. Kawai, A. Benassi, E. Gnecco, H. Söde, R. Pawlak, X. Feng, K. Müllen, D. Passerone, C. A. Pignedoli, P. Ruffieux, R. Fasel, E. Meyer, Science 2016, 351, 957.

[9] A. Tabarraei, S. Shadalou, J.-H. Song, Computational Materials Science 2015, 96, 10.

[10] S. M. M. Dubois, A. Lopez-Bezanilla, A. Cresti, F. Triozon, B. Biel, J.-C. Charlier, S. Roche, ACS Nano 2010, 4, 1971.

[11] D. W. Brenner, O. A. Shenderova, J. A. Harrison, S. J. Stuart, B. Ni, S. B. Sinnott, Journal of Physics: Condensed Matter 2002, 14, 783.

[12] A. Kınacı, J. B. Haskins, C. Sevik, T. Çağın, Physical Review B 2012, 86, 115410.

[13] I. Leven, I. Azuri, L. Kronik, O. Hod, The Journal of Chemical Physics 2014, 140, 104106.

[14] I. Leven, T. Maaravi, I. Azuri, L. Kronik, O. Hod, Journal of Chemical Theory and Computation 2016, 12, 2896.

[15] T. Maaravi, I. Leven, I. Azuri, L. Kronik, O. Hod, The Journal of Physical Chemistry C 2017, 121, 22826.

[16] W. Ouyang, D. Mandelli, M. Urbakh, O. Hod, Nano Letters 2018, 18, 6009.

[17] S. Plimpton, Journal of Computational Physics 1995, 117, 1.

[18] E. Bitzek, P. Koskinen, F. Gähler, M. Moseler, P. Gumbsch, Physical Review Letters 2006, 97, 170201.